ADVANCING EARTH AND SPACE SCIENCE

JGR Solid Earth

RESEARCH ARTICLE

10.1029/2019JB018145

On the Broadband Instrument Response of Fiber-Optic DAS Arrays

Nathaniel J. Lindsey[1,2,3], **Horst Rademacher**[1], **and Jonathan B. Ajo-Franklin**[2,4]

[1]Earth and Planetary Science Department, University of California, Berkeley, CA, USA, [2]Energy Geosciences Division, Lawrence Berkeley National Laboratory, Berkeley, CA, USA, [3]Geophysics Department, Stanford University, Stanford, CA, USA, [4]Department of Earth, Environmental, and Planetary Sciences, Rice University, Houston, TX, USA

Key Points:

- DAS instrument response for a telecom cable experiment is quantified empirically using a broadband seismometer
- Amplitude response is flat to true ground motion from 10–120 s but enhanced at shorter periods; phase response is flat from 1–120 s
- Our approach can be used to calibrate DAS arrays, enabling absolute ground motion amplitude measurements in the future

Supporting Information:

- Supporting Information S1

Correspondence to:
N. J. Lindsey,
natelindsey@berkeley.edu

Citation:
Lindsey, N. J., Rademacher, H., & Ajo-Franklin, J. B. (2020). On the broadband instrument response of fiber-optic DAS arrays. *Journal of Geophysical Research: Solid Earth*, *125*, e2019JB018145. https://doi.org/10.1029/2019JB018145

Received 5 JUN 2019
Accepted 17 JAN 2020
Accepted article online 23 JAN 2020

Abstract Distributed Acoustic Sensing (DAS) is a novel tool in array seismology that measures the phase of backscattered laser pulses traveling in a fiber-optic cable, and relates this measurement to the axial strain induced on the cable by a propagating seismic wavefield. Combining DAS with telecommunications optical fiber networks has begun to address a range of earth science questions where cost and field logistics have historically hindered observations. Unlike classic inertial seismometers, DAS instrument response is presently unquantified. This topic includes a variable sensing element—the fiber, including packaging and installation—which changes between experiments. Ignoring this element, one DAS record should approximate a fixed-length strain gauge, which exactly measures Earth's motion down to quasi-static frequencies relevant to geodesy. In this paper, we test this hypothesis using seismological observations of teleseismic earthquakes and microseism noise spanning the 1 to 120 s period range. We use a commercial DAS interrogator unit connected to an optical fiber previously used for telecommunication and a colocated broadband seismometer to estimate the DAS transfer function. We find a 1:1 correspondence with actual ground motion from 10–120 s. At shorter periods (1–10 s), DAS amplitude response is enhanced by 3–11 dB. Phase response is flat over this range of periods. We interpret the recovered DAS response function in terms of hypothesized fiber coupling and photonic effects. We propose this calibration methodology for future DAS experiments where seismic amplitude information is desired.

1. Introduction

The goal of all seismic measurements is to determine the true motion of the ground in response to mechanical vibrations. To be truly useful in studies of Earth's interior, seismic instruments must be able to record fine vibration amplitudes at the level of 1e−6 m/s ground velocity or smaller. Such precision is inherently difficult. Only various types of strainmeters, mechanical or optical, and Global Navigation Satellite System sensors can determine this movement directly (Agnew & Wyatt, 2003; Blum et al., 2008; Hohensinn & Geiger, 2018). In contrast, all inertial seismometers, by far the most common instruments used in seismometry, record the relative motion between the ground and a known internal inertial mass in response to vibrations (Lay & Wallace, 1995).

In order to relate these measurements to physical units of ground motion, the response characteristics of the inertial mass system must be known with as much precision as possible. Modern open-loop geophones and other short-period instruments, as well as electromechanical force-feedback broadband seismometers, are precisely described by empirical formula or as the numerical coefficients of a transfer function, commonly known as the instrument response function (Collette et al., 2012). Figure 1 shows the instrument response functions for four seismic instruments in common use today. Depending on the type of mechanical connection to the seismometer's frame, usually a leaf spring or another elastic device (Wielandt & Streckeisen, 1982), the system response can also show a phase shift with respect to the ground motion. Hence, inertial seismometer transfer functions commonly are documented in two parts, an amplitude response and a phase response. Instrument response functions are commonly derived from analytical methods or through calibration testing on shake and tilt tables (Hutt et al., 2009). Today, such response functions are well established for commercial instruments and typically are included in a parameterized form in the seismic recording metadata (IRIS-PASSCAL, 2019). Instrument response removal, a process akin to digital filtering, is a common numerical procedure available in open source libraries such as SAC (Goldstein et al., 2003) and ObsPy

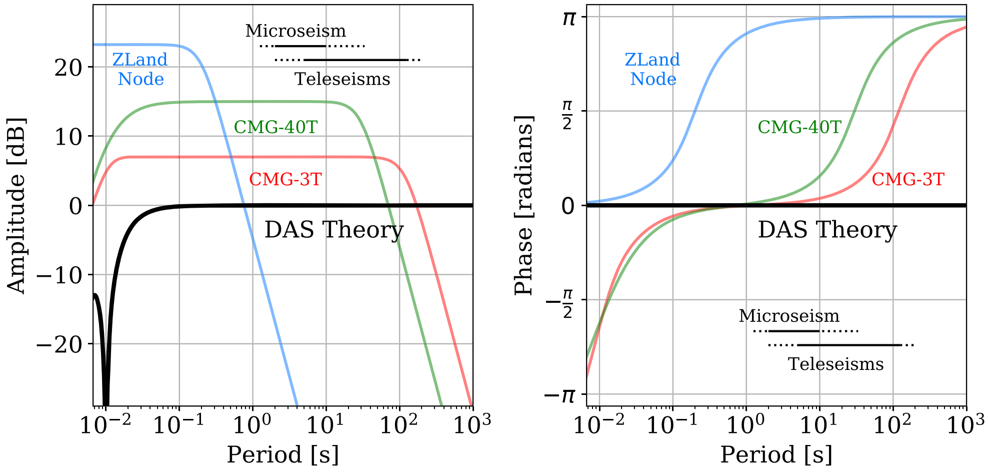

Figure 1. Instrument response functions for commonly used seismic instruments and DAS, including the CMG-3T (red) used in this study, CMG-40T (green), and ZLand Nodal geophone (blue). Amplitude functions are offset along the vertical axis for clarity; seismometers are plotted as dB with respect to V/m/s; the DAS is plotted as dB with respect to strain. Treating DAS as a strainmeter yields a theoretical DAS amplitude response, which falls to 0 due to the gauge length effect and is equal to 1 at the low-frequency limit.

(Beyreuther et al., 2010). This description only reflects the ideal case of a perfect coupling of the seismometer to the ground.

Distributed Acoustic Sensing (DAS) interrogators probe fiber-optic cables buried in the ground to measure the vibrations of their surroundings. While all manufacturers of inertial seismometers provide instrument response calibration information with each of their sensors, DAS system manufacturers do not all presently conform to a single standard. This has resulted in the assumption that DAS measurements are equivalent to an array of virtual fixed-dimension optical strain gauges popularized in the study of Earth motion at geodetic frequencies (Blum et al., 2008). The implication of this is that DAS data directly measure true ground motion at all frequencies subject to notches related to multiples of the gauge length (see Figure 1).

The broadband nature of DAS has largely been overshadowed by the use of DAS in active-source experiments at high frequencies ($f > 10$ Hz; $T < 0.1$ s). The long-period frequency response of the DAS method has been demonstrated in recordings of teleseismic earthquakes (Ajo-Franklin et al., 2019; Jousset et al., 2018) and laboratory and field pump tests (Becker et al., 2017; Becker & Coleman, 2019). To date, the longest period earthquake signal observed with DAS used a dark fiber DAS array in the Mojave Desert to capture propagating surface waves down to $T = 200$ s (Yu et al., 2019). Recently, Becker and Coleman (2019) showed that DAS can record tidal periods ($T = 4.3 \times 10^4$ s) in a laboratory setting, albeit with a strain amplitude 7×10^3 times greater than the solid Earth tide.

Generally, DAS studies have focused on seismic wave phase information, which is sufficient to model seismic wavefield velocities, for example, in vertical seismic profiling (Daley et al., 2016; Mateeva et al., 2014), ambient noise velocity inversions (Ajo-Franklin et al., 2019; Dou et al., 2017; Zeng et al., 2017), and earthquake phase identification (Ajo-Franklin et al., 2019; Jousset et al., 2018; Lindsey et al., 2017; Yu et al., 2019). However, true ground motion amplitudes are necessary for many other seismological processing tasks, including full-waveform inversion, AVO analysis, moment tensor inversion, and attenuation analysis, which the DAS community will likely investigate in the near future (Cole et al., 2018; Paitz et al., 2018).

This paper investigates how a telecommunications fiber-optic DAS array and a broadband inertial seismometer respond to the same input ground motion. We utilize a number of large ($M > 7$) teleseismic earthquakes and strong ocean microseism noise as the signals for the instrument comparison. Such an experiment enables estimation of DAS instrument response over the signal period range from $T = 1$–200 s with overlap of the two different types of seismic energy around 10 s. In section 2, we detail how photonic DAS measurements are made and the assumptions involved. In section 3, we describe the empirical deconvolution method to estimate DAS instrument response. In section 4, we describe the field experiment,

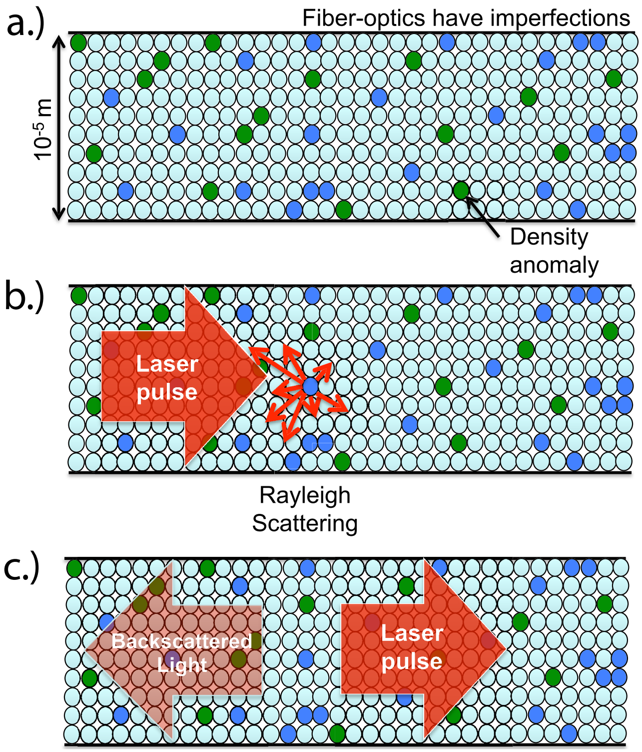

Figure 2. Conceptual cartoon of the DAS measurement principle: (a) Distribution of density anomalies in the core of standard-grade single-mode fiber-optic. (b) Rayleigh scattering of laser light occurs at unknown impurity locations. (c) As the laser pulse continues down the fiber, the backscattered light returns to the instrument. Photonic time-of-flight provides the mapping between measurements of optical phase change and distributed axial strain acting on incremental fiber sections.

data processing procedure, and earthquake and microseism noise observations. In section 5, we discuss the deconvolution results.

2. The DAS Measurement Principle

2.1. Background

DAS is the generic name given to a process in which a fiber-optic interrogator unit is used to measure the dynamics of a strain field acting on a fiber. This process can be accomplished using several distinct optical approaches; however, all commercial DAS instruments generate, send, and receive coherent laser light pulses to and from the fiber that it is attached to. Many DAS instruments utilize the principles of Rayleigh scattering to measure changes in photon path length. DAS is also called Distributed Vibration Sensing, Coherent Optical Time-Domain Reflectometery, Coherent Optical Frequency-Domain Reflectometery, or phase-sensitive Optical Time-Domain Reflectometery.

There are critical differences between some DAS instruments, which include whether the input signal is composed of one pulse or two, whether Rayleigh backscattering phase or amplitude information is analyzed, whether optical phase information is measured digitally or photonically, and whether such analysis is done in the time or frequency domain. Here, we restrict our focus to a single commercial instrument, the Silixa iDAS (Version 2), which is a time domain, single-pulse, phase-based DAS instrument (Parker et al., 2014). This particular DAS instrument is among the more widely utilized in the field of earthquake seismology (Ajo-Franklin et al., 2019; Jousset et al., 2018; Lindsey et al., 2017; Wang et al., 2018; Yu et al., 2019). The following discussion of the relationship between ground motion and DAS data is a synthesis of many works including Bakku (2015), Bóna et al. (2017), Dean et al. (2017), Grattan and Meggitt (2000), Hartog (2017), Kreger et al. (2015), Karrenbach et al. (2018), Masoudi and Newson (2016), Posey et al. (2000), Parker et al. (2014), and Willis et al. (2017), as well as U.S. patents on the technology (Farhadiroushan et al., 2009). Please see these resources for a superior discussion of specific instrument photonics, and the implications of alternative optoelectronic architectures.

2.2. Sending/Receiving Laser Pulses and Rayleigh Backscattering

Consider a DAS instrument connected to one end of a single-mode fiber. The connection is considered position $x = 0$. Assume the fiber has an average core refractive index of $n = 1.45$. A 40 ns duration near-infrared laser pulse with wavelength $\lambda = 1{,}550$ nm is sent into the fiber ($+x$ direction) at time $t = \tau_0$. Inside the fiber, these photons form a finite pulse approximately 8.28 m in length which moves at a predictable speed, $c_n = c/n = 3 \times 10^8/1.45 = 2.07 \times 10^8$ m/s.

Commercial-grade optical fiber is characterized by its constant refractive index within a precise tolerance; however, there are density variations in the doped silica glass of the fiber-optic core due to manufacturing and handling. These give rise to intrinsic and extrinsic Rayleigh scattering of a portion of the light pulse. The density variations or scattering locations are unknown, but their total distribution is assumed to be dense, homogenous, and time-invariant. Figure 2 illustrates this concept by shading the variations in refractive index. Based on the common telecommunications loss standard for Rayleigh scattering at 1,550 nm of 0.15 dB/km, the pulse described here is estimated to lose upward of a few thousand photons every meter, some of which are backscattered in the opposite direction and return to the instrument.

The outgoing pulse continues moving down the fiber out to a maximum fiber position, $x = x_{\max}$, which may be tens of meters to tens of kilometers away from the DAS instrument. No light travels beyond $x_{\max}$ because all photons have already been scattered or absorbed, or because $x_{\max}$ is the end of the fiber. In the latter case, optical attenuators are commonly used to mute any remaining light and prevent back-end reflection.

The backscattered energy returns to the instrument at a predictable time in the range $\tau_0 < t <= \tau_0 + 2 * x_{\max}/(c_n)$. Knowledge of $x_{\max}$ and c_n is used to delay the next laser pulse by the requisite amount of time in order to avoid optical interference between pulses.

2.3. Time-For-Distance Transform Locates Scatterers; Gauge Length Effect

The continuous backscattered signal recorded at the instrument is sampled every dt seconds for analysis. Although the scatterer locations are unknown, the jth backscattered signal arrival time, $t_j = \tau_0 + j \cdot dt$, is assumed to be a two-way traveltime over path length out to the scatter location $x = x_j$, which can be computed using c_n as in $x_j = j \cdot dt \cdot c_n/2$. This time-for-distance transform ultimately provides the mapping between the backscattered signal time series and the spatial coordinates of the DAS array data. Every location is described with a precision due to the uncertainty in the time-for-distance mapping such as $x_j \pm L_G/2$, where L_G is termed the gauge length. Note that the physical locations of channel position must still be determined, commonly by hammer "tap-test" surveying with input from as-built installation drawings of the fiber-optic route. Gauge lengths are conventionally a few meters to tens of meters and act as a low-pass filter on the strain field (Dean et al., 2017).

Gauge length has several important consequences for the recording of seismic waves, particularly when the seismic wavelength approaches the gauge length in value (Dean et al., 2017; Hartog, 2017; Martin et al., 2018). Depending on the optoelectronic design of the DAS instrument, the gauge length may be set by the hardware (internal reference loop length) or software (time lag between two pulses). If multiple laser wavelengths are used simultaneously, or if the raw backscattered signal is recorded and analyzed digitally, then the gauge length can be selected after acquisition (Hartog, 2017).

2.4. Optical Phase Change Measurement and Its Relationship to Fiber Strain

When a gauge length undergoes axial strain, how is the backscattered signal modified? Coherent light that has traveled a distance x in a material of refractive index n has a predictable phase measured in radians:

$$\Phi = \frac{4\pi n x}{\lambda}. \tag{1}$$

The DAS instrument presently discussed employs an optical interferometer to measure the optical phase change introduced by any path length change, $\partial\Phi/\partial t$. Recordings of $\partial\Phi/\partial t$ are made at the timescale of the laser repetition rate (Δt) such that $\partial\Phi/\partial t \approx \Delta\Phi/\Delta t$. The incremental phase change, $\Delta\Phi = \Phi(\tau_n + t_j, x_j) - \Phi(\tau_{n-1} + t_j, x_j)$, is assumed to be linearly represented by the expansion:

$$\Delta\Phi(t, x_j) = \frac{4\pi n L_G}{\lambda}\left[\frac{\Delta x}{x} + \frac{\Delta n}{n} + \frac{\Delta\lambda}{\lambda}\right], \tag{2}$$

where x_j represents the channel location in linear fiber length and $\frac{\Delta x}{x}$ represents the axial strain quantity of interest (Grattan & Meggitt, 2000). Hence, modifications in backscattering measured as $\Delta\Phi$ result from changes in fiber length ($\frac{\Delta x}{x}$) and also from changes in refractive index ($\frac{\Delta n}{n}$) or optical wavelength ($\frac{\Delta\lambda}{\lambda}$).

To isolate the axial strain effects, we will ignore optical dispersion ($\frac{\Delta\lambda}{\lambda} = 0$), because Rayleigh backscattering measurements are made at the incident wavelength ($\lambda = 1{,}550$ nm), and all other light can be filtered out of the system. Next, temperature changes can cause index of refraction changes (thermo-optical effect) and/or fiber length changes (thermal strain), but we assume that seismic wave strains the fiber over a timescale that is much faster than that of soil thermal fluctuations, which are driven by diurnal or seasonal cycles ($10^{-2} - 10^{2}$ s $\ll 10^{4}$ s). Stress can also induce changes in index of refraction (birefringence), but this is assumed to reduce to a scalar multiplicative factor (ζ) dependent on known material properties: $\zeta = 0.79$ for pure silica glass with an average Poisson's ratio of $\nu = 0.16$ at $\lambda = 1550$ nm (Schroeder, 1980). This value may be significantly lower ($\zeta = 0.735$) for light conducted through single-mode fiber glass, which contains GeO_2 dopants and interacts with cladding material (Bertholds & Dandliker, 1988). This analysis yields an expression for $\Delta\Phi$ that depends only on the dynamic mechanical strain (dilation or contraction) of an original fiber gauge length in the axial direction of the fiber, ϵ_{xx}, as in

$$\epsilon_{xx}(t, x_j) = \frac{\lambda}{4\pi n L_G \zeta}\Delta\Phi = \frac{1550 \cdot 10^{-9}\ (\mathrm{m})}{4\pi \cdot 1.445 \cdot 10\ (\mathrm{m}) \cdot 0.735}\Delta\Phi = 11.6 \cdot 10^{-9} \cdot \Delta\Phi\ (\mathrm{rad}). \tag{3}$$

In summary, the DAS system we consider injects laser light pulses into a fiber-optic cable and measures the backscattered signal's optical phase change over time by applying optical interferometry to consecutive backscattered signals, which yields array measurements of dynamic strain rate for individual fiber gauge lengths on the order of 10 m. The DAS recordings of dynamic strain can be contrasted with Brillouin-based fiber-optic strain techniques that measure the absolute strain acting on the cable but cannot (at present) record at high frequency or with similar levels of sensitivity (Kechavarzi et al., 2019).

As discussed in the introduction, there are alternative ways to measure $\Delta\Phi$. A different DAS instrument measures $\Delta\Phi$ between consecutive backscattered signals from the same laser pulse, $\Phi(\tau_n + t_j, x_j) - \Phi(\tau_n + t_{j-1}, x_j)$, instead of between consecutive pulses as described above, $\Phi(\tau_n+t_j, x_j)-\Phi(\tau_{n-1}+t_j, x_j)$. Because the time between consecutive laser pulses (10^{-5} s) is much greater than the time between backscattered signal samples (10^{-7} s), this alternative instrument records the $\Delta\Phi$ quantity instantaneously instead of recording the change in the quantity over the pulse repetition time. Thus, alternative instruments output data with native units of $\Delta\Phi$ rate instead of $\Delta\Phi$ as a convenience, but the measurements are underpinned by the same process.

2.5. Ground-to-Fiber Strain Transfer

DAS studies typically assume fiber-optic cables are rigidly and uniformly coupled to the Earth, a convenient formalism but not necessarily true (Kuvshinov, 2016; Mateeva et al., 2014). Exploration of DAS strain transfer issues first appeared in vertical seismic profiling experiments where free-hanging, clamped, and grouted fibers inside of oil and gas wells showed that data quality can depend systematically on the degree of rigid coupling (Hartog et al., 2014; Mateeva et al., 2014; Mestayer et al., 2011; Munn et al., 2017). Horizontally trenched direct burial and dark fiber installations face at least as many complications as vertical fiber installations, including the strain transfer through the fiber and cladding material; cable packing style (e.g., aramid synthetic fiber wrapped versus gel-filled with loose-tube); outer cable coating; conduit deployment versus direct burial; conduit material; degree of contact between the fiber and the conduit; occupancy of the conduit; number of conduits per trench; age; trench depth; drained versus undrained conditions. More work is required to understand these potential impacts, which certainly vary between dark fiber DAS experiments and likely also vary within each DAS array.

Laboratory investigations are beginning to provide a bottom-up understanding of how the isolated fiber-optic, or fiber cable package act as a sensing element (Becker et al., 2018; Papp et al., 2017). A few models have been proposed to upscale these results to seismic field data (Kuvshinov, 2016; Reinsch et al., 2017). Reinsch et al. (2017) proposes a simple multilayer model of one gel-filled/loose-tube fiber-optic embedded in a telecommunications grade cable buried in sand. The authors suggest that the small strain excited by earthquakes (1 μm/m) is within an elastic regime of both the ground-to-cable and cable-to-fiber systems. Based on the cable materials chosen, they calculate that seismic waves propagating at speeds in excess of 100 m/s (minimum soil V_s) are rigidly coupled to their surroundings below T $\sim$ 2s period.

2.6. Optical Noise

Array seismologists commonly average or stack N seismic records from different sensors to improve signal-to-noise ratios at a rate of $\sqrt{N}$ (Rost & Thomas, 2002). This technique assumes sensors record a correlated signal and uncorrelated noise. Local uncorrelated ground vibrations destructively interfere during stacking, but optical noise effects and stationary patterns of fiber coupling may not, or they may constructively interfere in a problematic fashion.

Several authors have observed local noise in DAS data, which we classify here. One type of noise, referred to as common-mode noise (Ajo-Franklin et al., 2019; Bakku, 2015; Dou et al., 2017) is characterized by an infinite-velocity signal (arrives at all channels simultaneously). This is caused by local seismic disturbance near the interrogator, which vibrates the optoelectronic system and leads to an overprinted signal on all channel recordings at the same time. Common-mode noise statistics thus depend on the local seismic disturbance and can appear quasi-random. To remove common-mode noise from a seismic data set, Bakku (2015) proposed utilizing a median filter in time; however, this may be problematic in real-time earthquake or other event detection algorithms, because normal-incident body waves arrive with near-infinite apparent velocity and are likely to be removed by such a median filter.

A second type of DAS noise characterized by a random infinite-velocity spike is attributed to laser frequency drift or laser noise (Zhirnov et al., 2016). This source of optical noise should be ameliorated over time as laser quality increases and can also be removed with a median filter.

A third type of optical noise manifests as a reduced amplitude pattern that is quasi-random in space but time invariant. This common problem in phase-sensitive Optical Time-Domain Reflectometery measurements is called optical fading (Gabai & Eyal, 2016). Generally speaking, fading results from destructive interference, which can happen when the random electric fields from scatterers within the fiber sum to a very small total magnitude (Hecht, 1998). This effect depends on the laser frequency, gauge length, and pulse width but will be time invariant for a chosen set of recording parameters. One demonstrated fading mitigation strategy employs multiple laser frequencies (Zhou et al., 2013). Reduced amplitude channel noise can also result from suboptimal fiber-ground coupling (Ajo-Franklin et al., 2019; Becker et al., 2017; Reinsch et al., 2017; Willis et al., 2017). Note that photonic fading noise and sensor coupling noise are difficult to distinguish except at the scale of the array, where sensor coupling is usually identifiable by its systematic pattern or from field installation information.

2.7. Self-Noise and Dynamic Range

Self-noise and dynamic range are also important response features of any seismic instrument. The minimum strain rate DAS measurement is ultimately determined by the optical energy or number of photons injected per pulse and the backscattering profile. The maximum strain rate level is set by the optical phase unwrapping algorithm applied inside of the instrument to recover the strain rate value, or the elasticity of the fiber itself (Hartog, 2017). Best practice for DAS parameter selection and instrument testing were provided by the joint industry forum (SEAFOM, 2018); however, specific instrument data sheets are not publically available at present. We do not consider dynamic range or self-noise in this paper; however, we do observe that the measured teleseismic ground motions (10^{-3} m/s) and microseism noise (10^{-5} m/s) are above the DAS self-noise.

3. Methodology

Propagating elastic waves are measured at the Earth's surface using a fiber-optic cable connected to a DAS instrument and a colocated seismometer. The seismometer is oriented in the fiber cable direction ($+x$ direction) and records the wavefield particle velocity v_x convolved with its known instrument response function $g(t)$. The DAS records the strain rate of the wavefield in the direction of the fiber axis ($\dot{e}_{xx}$), which we assume is convolved with an unknown DAS instrument response function $h(t)$. After integrating the DAS data to strain, the two measurements are related through the apparent phase velocity of the wave, c_x (Aki & Richards, 2002):

$$v_x(t) * g(t) = -c_x(x,t) * e_{xx}(x,t) * h(t). \tag{4}$$

After removing $g(t)$ from the seismometer data through standard instrument response removal, a Fourier transform is applied to all quantities. We express the DAS instrument response function in the frequency domain as

$$H(\omega) = \frac{V_x(\omega)}{-c_x(k_x,\omega)E_{xx}(k_x,\omega)}. \tag{5}$$

where $\omega = 2\pi/T$, $k_x = 2\pi/\lambda_x$, $X(\omega) = \mathcal{F}\{x(t)\}$.

The aim of this paper is to compare DAS and seismometer records to estimate $H(\omega)$. We focus on two different classes of seismic signal: (1) regional and teleseismic earthquakes with surface waves occupying a broad period range from 10–200 s and (2) weak ambient microseism noise excited by ocean-solid earth interactions and commonly recorded in continental interiors at periods shorter than the teleseism range (2–20 s). Other seismic wave types could also be utilized. Next, we describe how to estimate $H(\omega)$ using earthquakes or ambient noise.

3.1. Deconvolution of DAS Instrument Response

To determine the DAS instrument response, we must first convert the DAS strain and seismometer velocity values into a consistent format. Daley et al. (2016) showed how the array-nature of DAS can be used to convert DAS array strain values into particle velocity values in the frequency-wavenumber (FK) domain utilizing the phase velocity relation $c = \omega/k$. This FK-rescaling technique reformulates (5) as

$$H(\omega) = \frac{V_x(\omega)}{-(\frac{\omega+\eta}{k_x+\eta})E_{xx}(k_x,\omega)}. \tag{6}$$

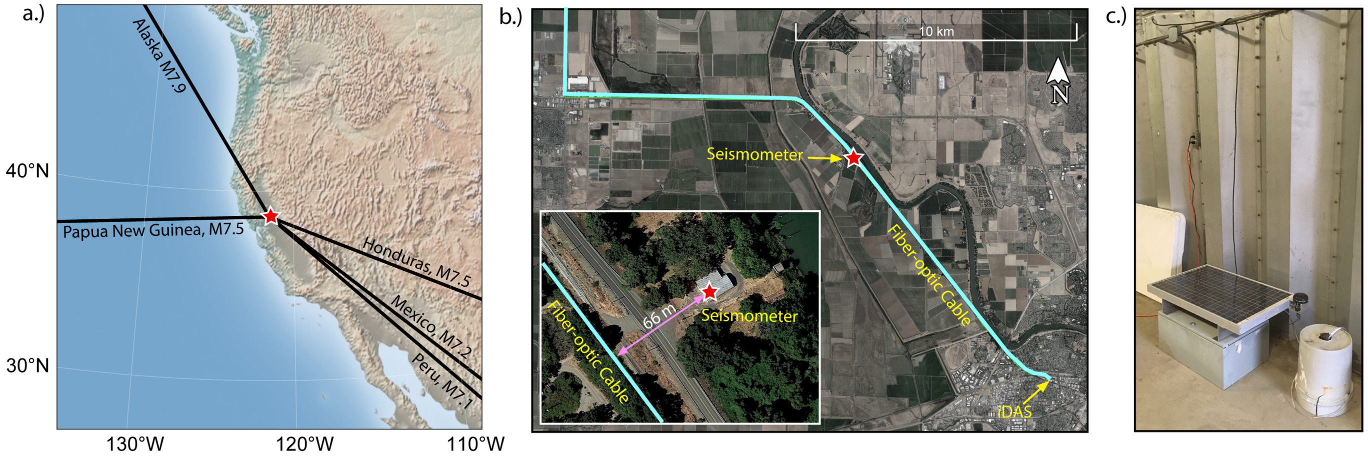

Figure 3. (a) Equal azimuth map projection of Western United Sates showing experiment location in Northern California with black lines indicating teleseism backazimuths (see Table 1). (b) Fiber-optic cable path or DAS array geometry for the FOSSA experiment showing location of the DAS instrument (Silixa iDAS) in West Sacramento, the seismometer (red star) about 9 km NW of the DAS instrument and 66 m NE of the fiber-optic cable. (c) Seismometer (Guralp CMG-3T) recording inside Elkhorn Fire Station. Sensor is sitting on a concrete pad, beside the gray box that contains the digitizer and battery.

Daley et al. (2016) applied the FK-rescaling technique to an active-source vertical DAS data set far from the free-surface and found a very good comparison with a vertical borehole geophone array. Wang et al. (2018) applied the technique to surface recordings of earthquakes where the propagating wavefield was observed to be strongly dispersive. Both studies assumed $H(\omega) = 1$ over the period range of interest ($T < 1$ s). The FK-rescaling technique may become unstable when the seismic wavefield is dominated by k_x values that approach 0. This may be problematic when teleseismic body waves arrive with near-vertical incidence on horizontal DAS arrays, or when surface waves arrive from a broadside backazimuth on a linear DAS array. To avoid the small number division instability, we numerically adjust the frequency and wavenumber values by the same η parameter (see supporting information for details).

4. Data

4.1. Field Experiment

For a period of 3 months beginning in November 2017, a three-component broadband inertial seismometer (Guralp CMG-3T; 750 V/m/s) was installed near a linear section of the Fiber-Optic Sacramento Seismic Array (FOSSA) experiment (Figure 3) documented in Ajo-Franklin et al. (2019). FOSSA utilized a commercial DAS instrument (Silixa iDAS, v.2, S/N 14033; Parker et al., 2014) with a 10 m gauge length. The DAS was connected to the southern end of an unlit single-mode long-haul telecommunications fiber-optic cable running from West Sacramento, CA, northwest to Woodland, CA. Continuous DAS recordings at 500 Hz sampling rate and 2 m channel spacing were made over the first 24 km of this fiber, resulting in a 12,000 horizontal strain rate component array. For additional details about the FOSSA experiment, please see the experiment description in Ajo-Franklin et al. (2019).

As described in detail in Ajo-Franklin et al. (2019), the FOSSA optical fiber was installed in 1999–2000 and some information about the fiber-soil coupling profile can be obtained from the as-built installation notes. The occupied 9/125 μm single-mode used to record DAS is one of 84 gel-filled, loose-tube Corning LEAF fibers inside one polythelene jacketed and steel-armored cables. This cable was pulled through a 4 cm diameter high-density polyethelene (HDPE) conduit (wall thickness = 0.5 cm) buried at 1–1.5 m depth in soil (backfilled and mechanically tamped). This cable and conduit were 1 of 12 in the same bundle. The section of the fiber presently analyzed was from Channel 4545 (9.09 km linear fiber length from the DAS instrument) to Channel 5045 (10.09 km).

The seismometer was installed on a concrete foundation inside the Elkhorn Fire Station southeast of Woodland, 66 m northeast from the midpoint of this fiber section. A digitizer and data logger (Guralp Minimus) were used to record the continuous inertial ground motion records at a 200 Hz sampling rate.

Unfortunately, both instruments experienced clock issues during the experiment. A 1 pps NPT time signal was provided to the DAS, but we could not obtain a GPS signal due to the location of the instrument inside

Table 1
Teleseismic Event Catalog Used in the DAS Instrument Response Analysis

Region	Mw	Origin time (UTC)	Distance	Backazimuth
Alaska	7.9	2018-Jan-23T09:31:43	2,778 km	302°
Mexico	7.2	2018-Feb-16T23:39:39	3,357 km	139°
Honduras	7.5	2018-Jan-10T02:51:31	4,355 km	130°
Peru	7.1	2018-Jan-14T09:08:45	7,088 km	141°
Papua New Guinea	7.5	2018-Feb-25T17:44:44	1,0804 km	231°

of a telecommunications point of presence facility. Relative clock differences between the two instruments were reduced using the maximum signal cross correlation of earthquake or nightly microseism recordings (see supporting information for details).

4.2. Observations

Global $M > 7$ earthquakes occurring during the FOSSA experiment (Table 1 and Figure 4a) provided coherent, body and surface wave phase arrivals. DAS records were used to identify major phases; however, in some

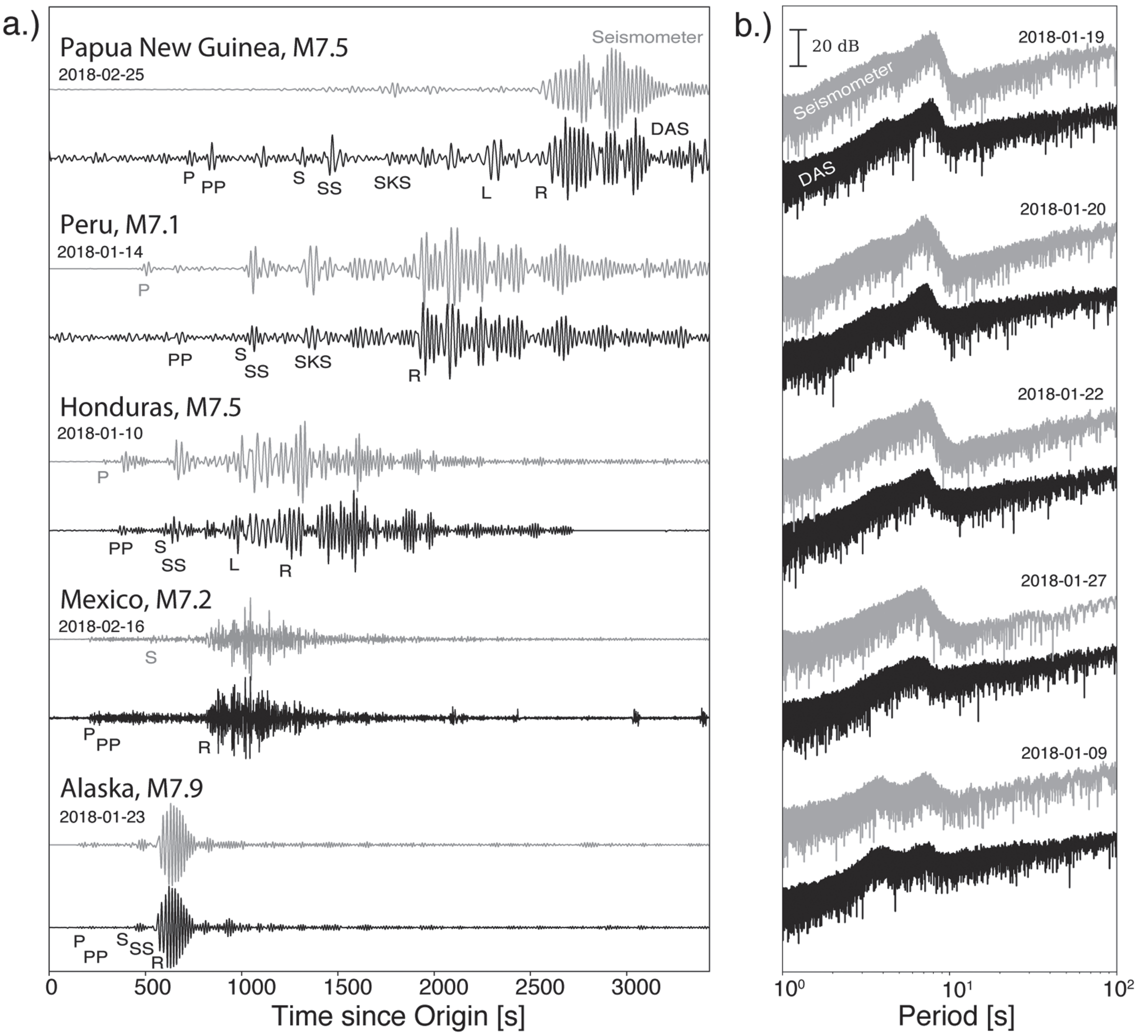

Figure 4. Teleseism and microseism ground motions highlight the general similarity between DAS and broadband seismometer signals over a wide period range. Note that DAS data are strain and seismometer data velocity. (a) Teleseismic event waveforms with dominant period range 20–100 s normalized by event (black = DAS, strain; gray = seismometer, velocity). (b) Nightly microseism noise power spectral density with peak period around 5–8 s (black = DAS, velocity; gray = seismometer, velocity; 23:00–07:00 local time). DAS record earthquake phase picks are labeled below the DAS trace, unless the phase was only visible on the seismometer.

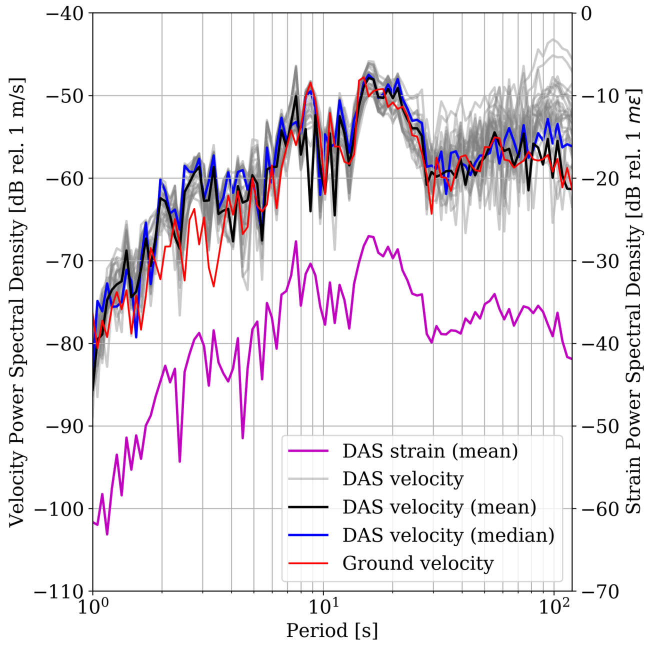

Figure 5. Effect of FK-rescaling process on DAS recorded strain amplitude spectra for the 23 January 2018 Alaska M7.9 event. Red line is true horizontal ground velocity as measured by a broadband seismometer component in the direction of the fiber-optic cable. Pink line is mean DAS strain from five gauge lengths (±50 m or 25 channels) of the cable centered around the DAS channel closest to the seismometer. Gray lines are DAS channel velocity spectra from these five gauge lengths, plotted with lines representing the mean (bold black line) and median velocity spectra (bold blue line). We use the mean five gauge DAS velocity in comparisons with the seismometer.

cases the P wave phase was only visible on the seismometer record. Event backazimuths ranged from near the axis of the fiber-optic cable to orthogonal to the fiber (Figure 3a). Due to the proximity of the FOSSA dark fiber DAS experiment to a railway, local train noise disrupted some of the earthquake event recordings: Alaska M7.9 and Honduras M7.5 were not disrupted; the recording of Peru M7.1 was limited to 400 s; Papua New Guinea M7.5 was limited to 575 s; Mexico M7.2 was not usable. The seismic waves from these events were observed to have energy in the period range $T = 1$–120 s, with the strongest amplitudes occurring at periods longer than $T = 20$ s.

To corroborate the analysis of DAS response around $T = 10$ s period and expand the spectral range to shorter periods, we analyzed observations of ambient microseism noise. At our site, microseism noise has higher-frequency content than the teleseismic signals, covering the range from $T = 1$–10 s. We restrict our analysis to the 10 nights of microseism noise during the FOSSA experiment time period based on a survey of probabilistic power spectral density across the Northern California Seismic Network. Data from 00:00–00:25 local time (UTC+7) were chosen in order to reduce the level of anthropogenic noise. Figure 4b shows five nightly noise records for both instruments (DAS, 1 channel = black; seismometer, rotated into fiber azimuth = gray). Nightly spectral characteristics and night-to-night amplitude variations are consistent between the two sensing approaches. For example, there is a systematic fall-off in power spectral density away from the secondary microseism peak around 4–8 s. DAS records show stronger spectral response to ambient noise at higher frequencies relative to the seismometer.

4.3. Seismometer Data Processing

Seismometer data processing involved a linear detrending step, followed by mean subtraction and application of a symmetric Hanning window taper. Next, we removed the calibrated instrument response function and digitizer bitweight provided by the vendor to transfer the seismometer data from raw units of V/m/s into ground velocity units. This included accounting for the seismometer's sensitivity. This seismometer's transfer function is characterized by a flat response in amplitude and phase over the period range 0.02–120 s (see curves for CMG-3T in Figure 1). Then, we rotated the data from the recording frame orientation (NEZ) into the fiber-oriented reference frame (TRZ; radial = 142°N) to retrieve the true horizontal ground velocity component aligned with the fiber. Finally, we applied a zerophase, two-corner, band-pass filter. For teleseismic analysis we filtered the data from $T = 1 - 200$ s. For microseism noise analysis we filtered the data from $T = 0.5 - 20$ s.

4.4. DAS Data Processing

DAS data processing involved converting raw optical phase change to strain rate using the standard conversion value of $11.6 \cdot 10^{-9}$ nanostrains/radian (see equation (3)), followed by linear detrending, mean subtraction, and tapering, identical to the seismometer workflow described above. Next, we integrated the DAS data to convert from strain rate to strain units and applied the same bandpass filter described above. We then applied the FK-rescaling algorithm described in section 3.1 using a DAS section of 100 gauge lengths, equivalently 500 channels or 1 km, centered on the DAS channel closest to the seismometer.

As described in section 3 and equation (6), the FK-rescaling algorithm has a numerical instability for low wavenumber seismic phases. The interested reader is referred to the supporting information, where we describe how we select the scalar water level parameter η, which is added to numerator and denominator of the phase velocity term prior to rescaling to avoid this issue.

The effects of these data processing steps on the recorded DAS spectra are illustrated in Figure 5 for an example earthquake record. Averaging the rescaled DAS channel data over five gauge lengths, equivalently 25 channels or 50 m, was found to yield a DAS velocity record that could be closely compared with the velocity spectra recorded by the seismometer. We used the five gauge lengths (±50 m or 25 channels) of the fiber-optic cable in Sacramento centered on the DAS channel closest to the seismometer. This stacking procedure had

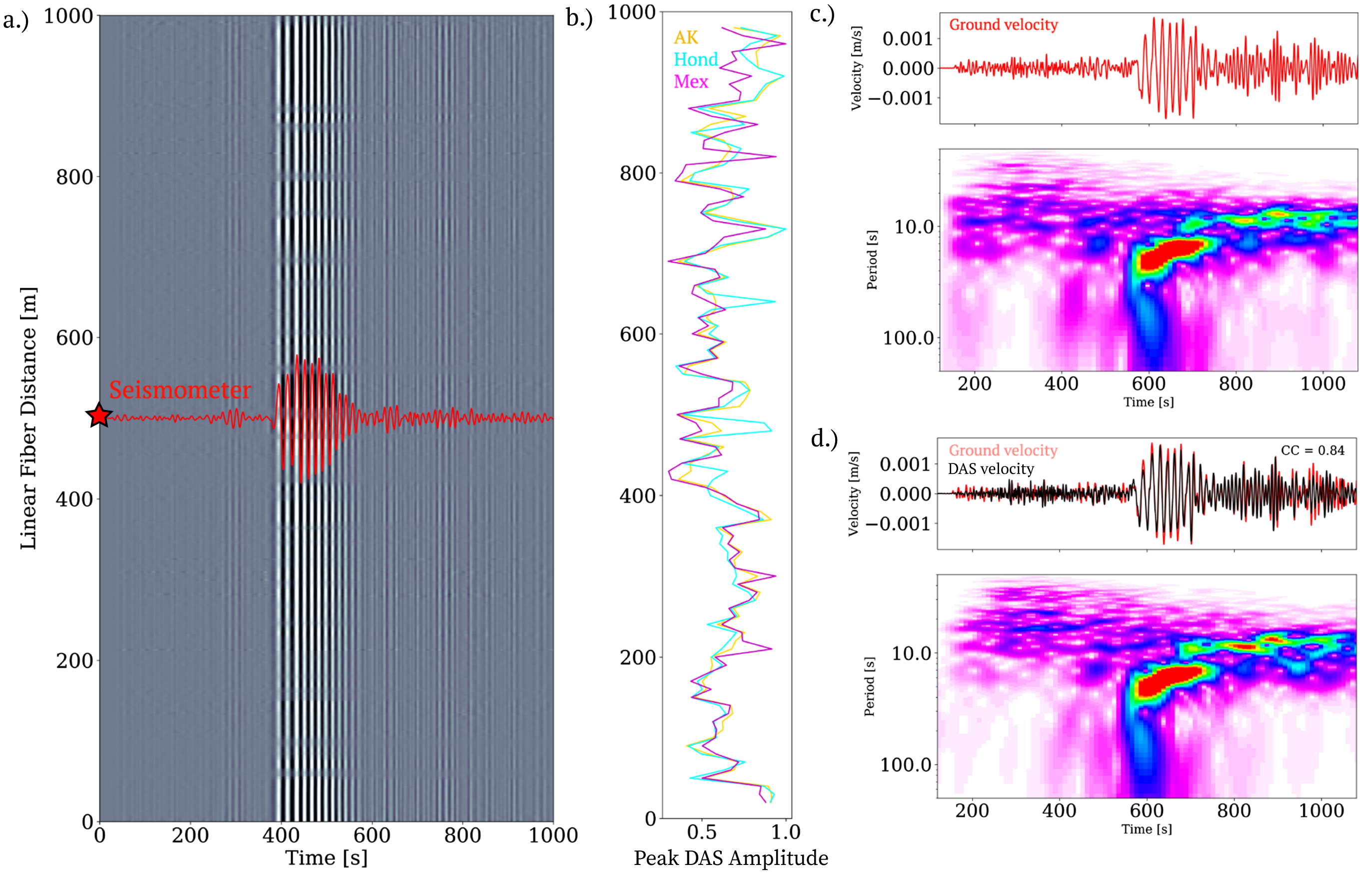

Figure 6. Observed ground motion velocities for 23 January 2018 Alaska M7.9 event. (a) The 500 DAS velocity records after FK-rescaling (black/white image) centered on the location of the seismometer record (red star and seismogram; band-pass filter = 10–100 s, *p* 2, *n* 4). (b) Maximum DAS amplitude versus position in a. after gauge-averaging for three separate teleseismic earthquakes (gold = Alaska; cyan = Honduras; magenta = Mexico). Systematic amplitude variability is interpreted as photonic fading. (c) Horizontal ground velocity record and time-frequency spectrogram from the fiber-oriented seismometer component; no filter. (d) Same as (c) but for the average of DAS velocity records shown in (a). Both instruments retrieve the strong dispersive Rayleigh wave with long-period airy phase arriving at 550 s; DAS shows a stronger response for $T \leq 10$ s.

the advantage of decreasing decorrelated noise and increasing fidelity of the long wavelength signals that are the subject of interest in this study. It also provided a local distribution of instrument response results that we represent using error bars in the results below. Stacking DAS channels beyond five gauge lengths was not found to substantially modify waveforms. Distant earthquakes and microseism noise excite long-period ground motions with wavelengths in excess of λ=500 m. Therefore, we can safely stack neighboring DAS records without sacrificing fidelity. Indeed, Figure 6a demonstrates that the 23 January 2018 Alaska M7.9 teleseismic earthquake wavefield propagates with coherence length scales much greater than 1 km.

For the Alaska event recording shown in Figure 6, time-invariant amplitude reductions of more than 50% of the peak amplitude were registered at some DAS channels with a quasi-random pattern. Similar fading patterns were observed for two different teleseismic events that occurred weeks later (Figure 6b). Alternatively, the observed localized amplitude reductions could result from insufficient coupling or local geology, but we hypothesize that such effects would exhibit a more ordered pattern than was not observed. For example, coupling effects should correlate with install condition (e.g., steel versus plastic conduit) or manifest as a fixed length scale effect related to the twist of the cable inside the conduit. Local geological effects might correlate with distance from the river. However, there is no variation in coupling or local geology over this kilometer based on available information. To mitigate the impact of fading in this analysis, we relied on waveform stacking. Although photonic fading was problematic, common-mode noise issues appeared to be minimal for our experiment.

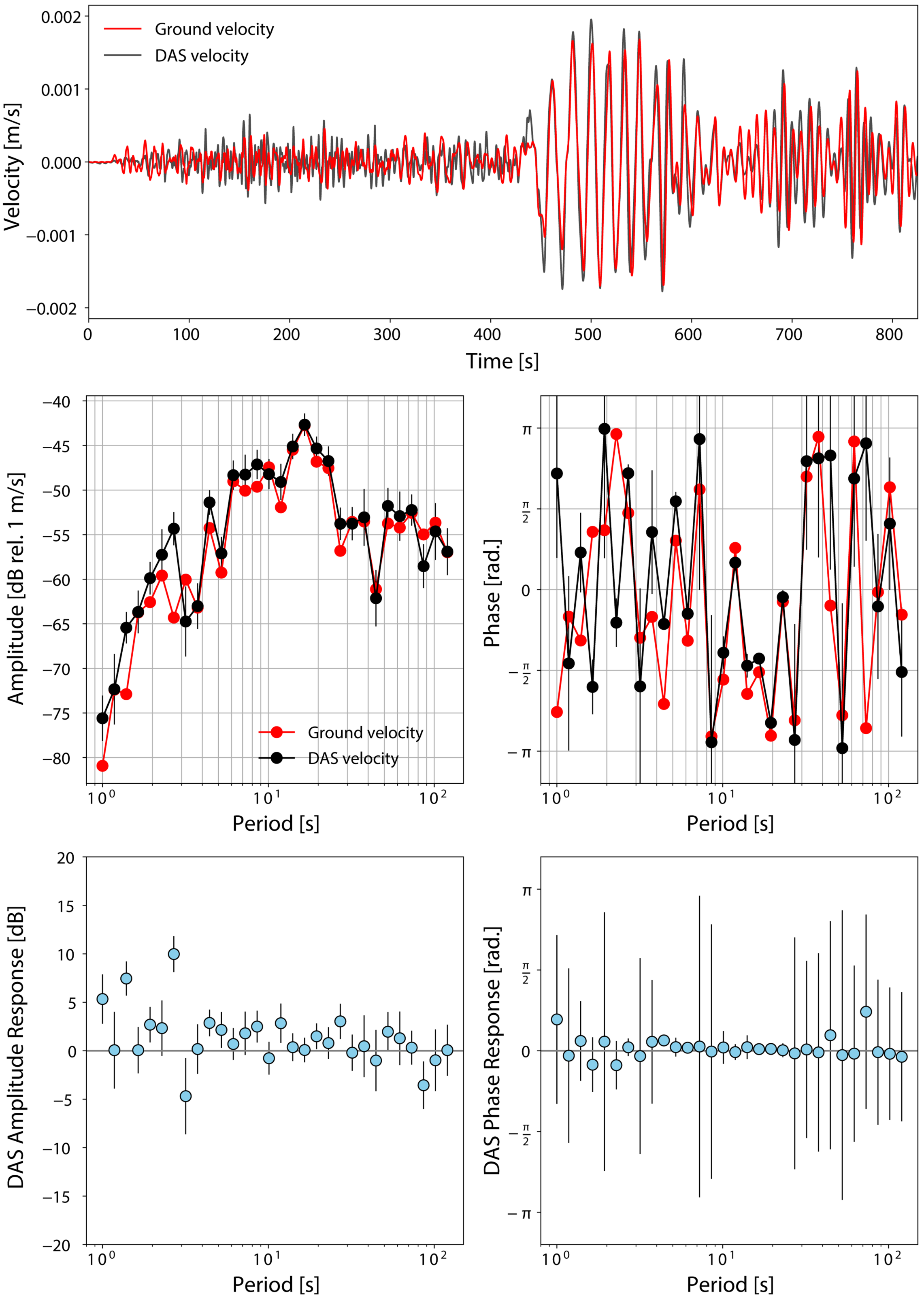

Figure 7. DAS instrument response deconvolution analysis for the 23 January 2018 Alaska M7.9 event records. (top) Waveform comparison of ground velocity from the seismometer (black) and DAS equivalent velocity (red). (center) Amplitude and phase spectra for two records before deconvolution. (bottom) Resulting DAS amplitude and phase response spectra after deconvolution. Black line indicates theoretical DAS instrument response shown in Figure 1. The 2-sigma error bars are plotted from the DAS channel distribution used for averaging.

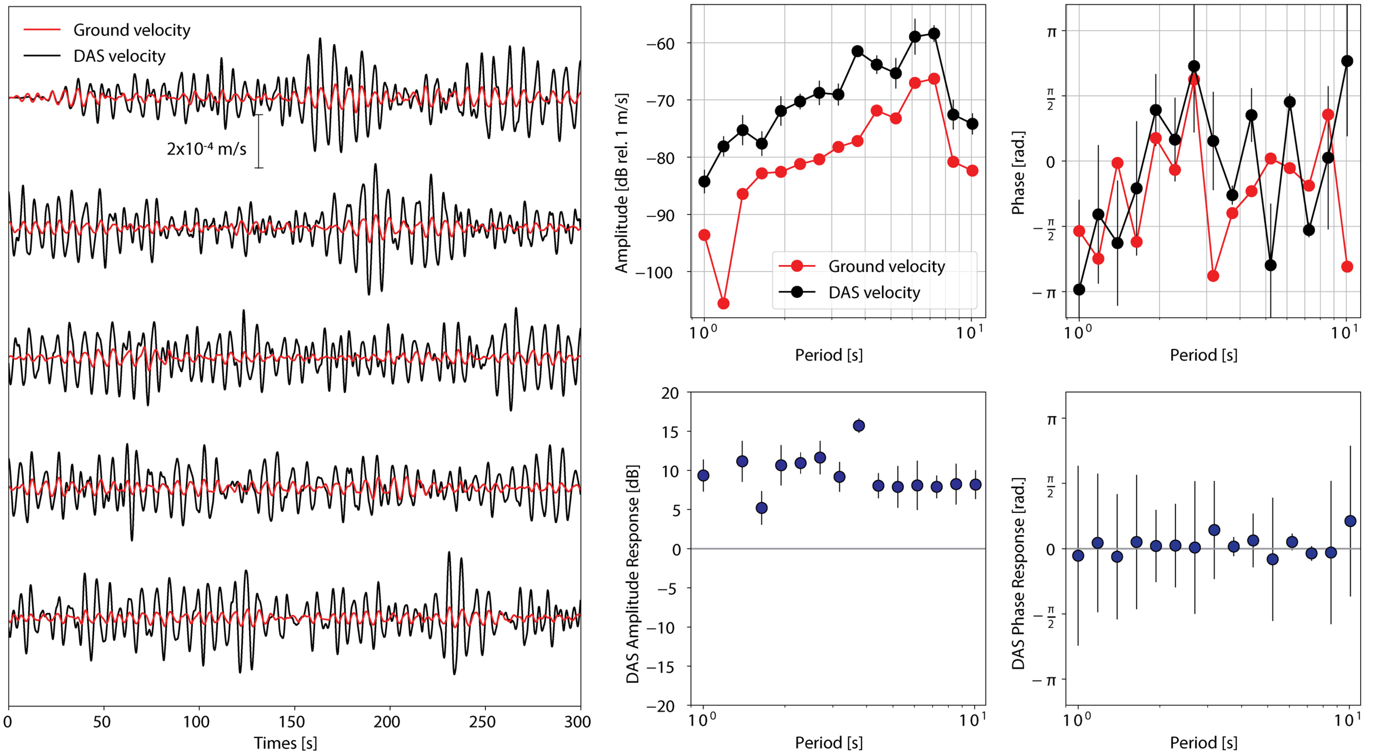

Figure 8. DAS instrument response deconvolution analysis for microseism noise from the night of 19 February 2018. (left) Waveform comparison of ground velocity from the seismometer (black) and DAS equivalent velocity (red). (top Left) Amplitude and phase spectra for two records before deconvolution. (bottom Left) Resulting DAS amplitude and phase response spectra after deconvolution. Black line indicates theoretical DAS instrument response shown in Figure 1.

5. Results

Using the 23 January 2018 Alaska M7.9 earthquake as an example, we found that after the conversion to comparable velocity units the DAS and seismometer recordings showed many important similarities. First, time-frequency analysis (Figures 6c and 6d) showed that the shape of the highest-energy fundamental Rayleigh wave was captured by both instruments. This included the long-period airy phase down to $T = 300$ s. In general, the timing and relative energy of body wave phases before the dominant Rayleigh wave as well as subsequent scattering were well matched. However, the DAS record of the *P* wave amplitude was almost a factor of ten lower than the inertial component record, as predicted from azimuthal sensitivity differences of the two instruments (Kuvshinov, 2016). Late-arriving relatively high frequency surface waves with dominant energy around 8–12 s were more strongly recovered by the DAS than the seismometer.

Frequency domain deconvolution of the 23 January 2018 Alaska M7.9 DAS record by the seismometer's record of true ground motion resulted in the empirical estimate of DAS instrument response shown in Figure 7. DAS phase response was approximately identical to the broadband seismometer, and DAS amplitude response was also approximately identical to the broadband seismometer with increasing response in the range 1–10 s. These findings are verified with time domain evidence of highly correlated, in-phase waveforms, equal amplitude response levels at longer periods, and elevated DAS amplitude response levels at shorter periods. Error bars (2-sigma) representing the distribution in DAS channel records from the five gauge length used for averaging demonstrate that the uncertainty increases when the seismic signal amplitude decreases. Instrument response estimates outside the range 1–120 s were limited by signal energy. Similar empirical estimates of the DAS instrument response for this segment of the Sacramento FOSSA experiment were retrieved using recordings of the 10 January 2019 Honduras M7.5, 14 January 2018 Peru M7.1, and 25 February 2018 Papua New Guinea M7.5 events (see supporting information). The 30–120 s estimates for the Peru event were not considered because the seismometer registered unreasonably low response.

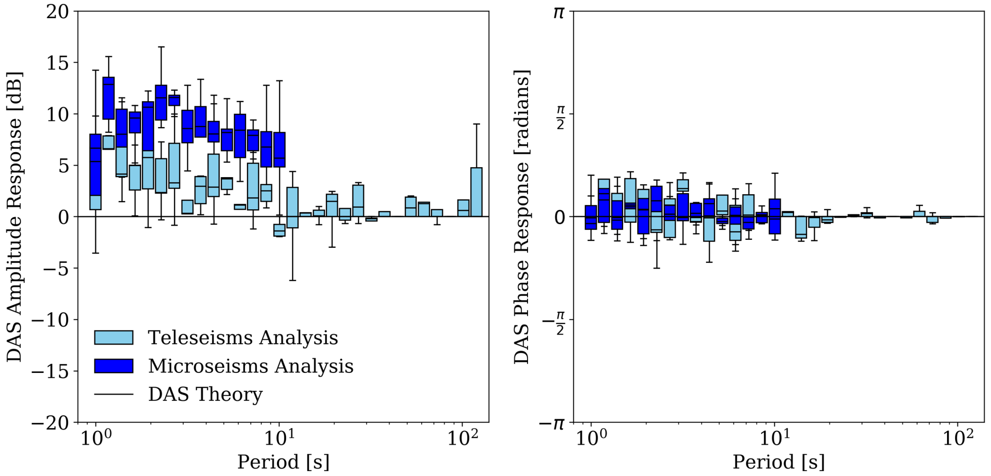

Figure 9. (left) Amplitude and (right) phase parts of DAS instrument response function estimated using teleseisms (light blue) and noise (dark blue). Distribution of teleseism comparisons for the Alaska, Honduras, Peru, and Papua New Guinea events and 10 nights of microseism noise are represented by box-and-whisker plots illustrating minimum, first quartile, median, third quartile, and maximum values as a function of signal period. Black line indicates theoretical DAS instrument response shown in Figure 1.

Additional estimates of DAS instrument response from short period ocean microseism noise around 1–10 s also result in a flat DAS phase response, and an elevated DAS amplitude response, which is in agreement with the teleseismic analysis (Figure 8). Observing this signal period range in the time domain, as in the left panel of Figure 8, the DAS is clearly responding with higher sensitivity when compared with the seismometer.

Figure 9 summarizes the empirical estimates made using four major teleseisms and 10 nights of strong ocean noise. DAS amplitude response is flat to ground motion from $T = 10$–120 s but increases from 10 to 1 s. DAS amplitude response level over 1–10 s is 3–11 $\pm$ 2 dB higher than true ground motion. The teleseisms analysis results in a higher DAS amplitude response (5–11 dB) compared with the microseisms analysis (3–7 dB). DAS phase response is flat from 1–120 s with slight increase in uncertainty over 1–10 s, possibly related to reductions in the amplitude of propagating seismic energy at shorter periods.

6. Discussion

To date, DAS studies have largely analyzed high frequency seismic signals ($T < 1$ s), with only a few studies presenting evidence of the long-period response of DAS. According to our results, the broadband DAS response is validated against a high-quality broadband seismometer over the range from 1–120 s. In terms of frequency range, DAS is found to be as broadband as the broadband seismometer used for calibration. Usable teleseismic energy falls off at periods longer than 120 s, but the DAS continues to show energy in time-frequency analysis down to 300 s. This is more than twice as long as the longest period DAS signals previously documented by Becker et al. (2017) in a hydrogeological pump test and in earthquake studies on dark fiber DAS arrays (Ajo-Franklin et al., 2019; Yu et al., 2019). One reason for this may be the DAS data processing approach employed here in which we stack over a window of 50 m, all falling inside of the seismic wave's long coherence length, mitigating uncorrelated channel noise and improving recovery of low frequency signals.

According to our results, the DAS instrument response function, parameterized as amplitude and phase response coefficients relative to true ground motion over the period range 1–120 s, can be estimated by frequency domain deconvolution using a seismometer velocity record as the observation of how the ground moved. The resulting function is empirical and, as such, has the shortcoming that it cannot, in isolation, be used to rationalize or separate fiber sensing element effects from optoelectronic effects. Furthermore, our quantification of the Sacramento array instrument response may or may not be applicable to other DAS field experiments. The central advantage of this approach is that after conducting this simple test DAS data can be reduced to true ground motion data, which can be relied upon for accurate wavefield amplitude measurements, in addition to phase (traveltime) measurements.

To our knowledge, no previous evidence of DAS instrument response calibration exists. Our results conclude that DAS amplitude response is flat over the period range 10–120 s, which agrees with theoretical prediction that the combined optoelectronic/fiber DAS system operates as a linear strainmeter. At periods shorter than 10 s, multiple lines of evidence suggest that DAS amplitude response increases to 3–11 dB above true ground motion. The effect is less pronounced for teleseisms than for microseism noise, potentially as a result of the FK-rescaling algorithm's behavior with seismic waves arriving nearly broadside from the coast, or with low energy microseism noise observations.

Elevated DAS amplitude response at short periods could be caused by the style and degree of rigid coupling through which strain is transferred from the ground to the fiber. Coupling is a necessary condition for any seismometer (Lay & Wallace, 1995), yet many DAS studies have concluded that mechanical coupling of the fiber-optic to the ground had an impact on their results (Becker et al., 2017; Jousset et al., 2018; Lindsey et al., 2017; Wang et al., 2018; Willis et al., 2017; Yu et al., 2019). Coupling is a static feature of a DAS experiment (fiber array; DAS recording parameters) that should be assumed to not change over the duration of a typical geophysical campaign (days to months). In vertical wells, grouting the fiber behind the well casing or using a pressurized permeable sleeve in uncased wells has been shown to improve strain transfer for DAS measurements (Becker et al., 2017). The topic of coupling horizontally oriented dark fiber experiments that involve a wide-diameter fiber cable bundle and PVC or HDPE conduit surrounding the fiber has received less attention. Ajo-Franklin et al. (2019) observed that in the FOSSA experiment three different conduit styles described by the telecommunications company drawings had a first-order impact on regional dark fiber DAS earthquake waveform recordings. However, Hooke's Law predict >99% strain transfer for a simple fiber embedded in sand excited by a long-period ground motion with wavelength 20 m (Reinsch et al., 2017). We expect that the HDPE conduit material used at FOSSA would modify the amplitude response uniformly over the period range considered (1–120 s) but may impact the response at shorter wavelengths where the length scale of the wave approaches that of the conduit. A flat phase response suggests the fiber-conduit system behaves in a linear elastic regime of strain transfer. We find no evidence for a viscoelastic rise time required to activate the DAS cable as proposed by Kuvshinov (2016). This may be due to the aramid-wrapped fiber or drained soil conditions surrounding the conduit in the FOSSA experiment. Gel-filled fibers or subsea or undrained cable conditions may act differently. Calibration of DAS instrument response in a direct fiber experiment may clarify the conduit's effect. The uptick in DAS amplitude response at $T < 10$ s could be related to the mechanical coupling of the conduit-ground system.

Future evaluation of other DAS arrays and other DAS instruments is necessary to understand the wider applicability of the present conclusions about DAS instrument response. An ultimate aim of future laboratory and field experiments will be to summarize DAS instrument response as a set of poles and zeros representing the instrumental transfer function. The present study shows that the instrument response should include both the photonic and fiber characteristics as a single system, with potentially important factors including the particular optical interferometry setup, fiber type, cable packaging, and conduit coupling.

7. Conclusions

DAS instruments enable acquisition of spatially dense recordings of propagating seismic wavefields by sampling the strain field along fiber-optic cables. The DAS method sends and receives laser pulses in the fiber and measures how the optical phase of coherent Rayleigh backscattering from positions along the fiber changes through time. DAS instrument response has not been rigorously analyzed, especially at $T > 1$ s. In this study, we used a precisely-calibrated broadband inertial seismometer located along a dark fiber DAS transect to measure the true ground motion exciting the fiber and use these measurements to solve for the broadband ($T = 1$–120 s) amplitude and phase response of a widely used commercial DAS interrogator. We used teleseismic earthquakes and multiple periods of ocean microseism noise as the input signals to probe the DAS instrument response function. As demonstrated by our results, the DAS frequency range is as broad as the broadband seismometer used in the analysis. The recovered DAS amplitude response is flat with respect to true ground velocity in the range 10–120 s but is elevated at shorter periods potentially due to coupling. DAS phase response is flat over the entire range of investigation.

Additional field and laboratory studies are necessary to clarify DAS parameters, including frequency range, instrument response, minimum sensitivity, self-noise, and dynamic range, as well as separate photonic and cable effects, and characterize other important aspects of this new form of seismometery. The instrument comparison methodologies proposed in this work could be applied to other DAS experiments with other DAS instruments as means of interarray calibration, specifically to understand the observed differences between the recorded DAS amplitude and true ground motion.

Acknowledgments
Data access is provided under the common Enabling FAIR data Project guidelines at the Northern California Earthquake Data Center via anonymous (ftp: http://www.ncedc.org/ftp/outgoing/Papers/2019_Lindsey/). N. Lindsey was supported by the National Science Foundation Graduate Research Fellowship under Grant DGE 1106400. The experiment was made possible by the Laboratory Directed Research and Development (LDRD) Program of Lawrence Berkeley National Laboratory under U.S. Department of Energy Contract DE-AC02-05CH11231, which also supported J. Ajo-Franklin. The ESnet Dark Fiber Testbed used in this project was supported by the Office of Science of the U.S. Department of Energy under contract DE-AC02-05CH11231. We would like to thank ESnet personnel including Inder Monga and Chris Tracy for their support in the original FOSSA experiment. We would like to thank Silixa for long-term partnership in support of our DAS acquisition efforts, and Guralp for their assistance in data handling. CenturyLink provided installation protocol details on the network and fiber section utilized in this study. Access to the broadband seismometer installation site was provided by the Chief Yuong at the Elkhorn Fire Department. Obspy and Matplotlib were used for seismic data analysis and plotting. Our effort was improved by insightful comments of Doug Dreger, Barbara Romanowicz, Taka'aki Taira, and Eileen Martin. We would like to thank the Editor, André Revil, Philippe Jousset (GFZ), the technical team at Silixa, Aleksei Titov (Colorado School of Mines), and one anonymous reviewer for their constructive feedback. NSF, GRFP Grant 1106400, LBNL, LDRD Grant DE-AC02-05CH11231.

References

Agnew, D. C., & Wyatt, F. K. (2003). *Long-base laser strainmeters: A review*. UC San Diego: Scripps Institution of Oceanography.

Ajo-Franklin, J. B., Dou, S., Lindsey, N. J., Monga, I., Tracy, C., Robertson, M., et al. (2019). Distributed acoustic sensing using dark fiber for near-surface characterization and broadband seismic event detection. *Scientific reports*, *9*(1), 1328.

Aki, K., & Richards, P. G. (2002). *Quantitative seismology* (2nd ed.). San Francisco: University Science Books.

Bakku, S. K. (2015). Fracture characterization from seismic measurements in a borehole (Ph.D. Thesis), Massachusetts Institute of Technology.

Becker, M. W., Ciervo, C., Cole, M., Coleman, T., & Mondanos, M. (2017). Fracture hydromechanical response measured by fiber optic distributed acoustic sensing at millihertz frequencies. *Geophysical Research Letters*, *44*, 7295–7302. https://doi.org/10.1002/2017GL073931

Becker, M. W., Ciervo, C., & Coleman, T. (2018). Laboratory testing of low frequency strain measured by distributed acoustic sensing, *SEG technical program expanded abstracts 2018* (pp. 4963–4966). Society of Exploration Geophysicists.

Becker, & Coleman, T. (2019). Distributed acoustic sensing of strain at earth tide frequencies. *Sensors*, *19*(9), 1975.

Bertholds, A., & Dandliker, R. (1988). Determination of the individual strain-optic coefficients in single-mode optical fibres. *Journal of lightwave technology*, *6*(1), 17–20.

Beyreuther, M., Barsch, R., Krischer, L., Megies, T., Behr, Y., & Wassermann, J. (2010). ObsPy: A Python toolbox for seismology. *Seismological Research Letters*, *81*(3), 530–533.

Blum, J. A., Nooner, S. L., & Zumberge, M. A. (2008). Recording Earth strain with optical fibers. *IEEE Sensors Journal*, *8*(7), 1152–1160.

Bóna, A, Dean, T, Correa, J, Pevzner, R, Tertyshnikov, K., & Van Zaanen, L (2017). Amplitude and phase response of DAS receivers. In *79th eage conference and exhibition 2017*.

Cole, S., Karrenbach, M., Kahn, D., Rich, J., Silver, K., & Langton, D. (2018). Source parameter estimation from DAS microseismic data, *SEG technical program expanded abstracts 2018* (pp. 4928–4932): Society of Exploration Geophysicists.

Collette, C., Janssens, S., Fernandez-Carmona, P., Artoos, K., Guinchard, M., Hauviller, C., & Preumont, A. (2012). Inertial sensors for low-frequency seismic vibration measurement. *Bulletin of the seismological society of America*, *102*(4), 1289–1300.

Daley, T., Miller, D., Dodds, K, Cook, P, & Freifeld, B. (2016). Field testing of modular borehole monitoring with simultaneous distributed acoustic sensing and geophone vertical seismic profiles at Citronelle, Alabama. *Geophysical Prospecting*, *64*(5), 1318–1334.

Dean, Cuny, & Hartog (2017). The effect of gauge length on axially incident P-waves measured using fibre optic Distributed Vibration Sensing. *Geophysical Prospecting*, *65*(1), 184–193.

Dou, S., Lindsey, N., Wagner, A. M., Daley, T. M., Freifeld, B., Robertson, M., et al. (2017). Distributed acoustic sensing for seismic monitoring of the near surface: A traffic-noise interferometry case study. *Scientific reports*, *7*(1), 11620.

Farhadiroushan, M., Parker, T. R., & Shatalin, S. (2009). Method and apparatus for optical sensing. WO2010136810A2.

Gabai, H., & Eyal, A. (2016). On the sensitivity of distributed acoustic sensing. *Optics letters*, *41*(24), 5648–5651.

Goldstein, P., Dodge, D., Firpo, M., Minner, L., Lee, W., Kanamori, H, et al. (2003). SAC2000: Signal processing and analysis tools for seismologists and engineers. *The IASPEI International Handbook of Earthquake and Engineering Seismology*, *81*, 1613–1620.

Grattan, K., & Meggitt, B. (2000). *Optical fibre sensor technology: Advanced applications-Bragg gratings and distributed sensors*. London, UK: City University.

Hartog, A. (2017). *An introduction to distributed optical fibre sensors*. Boca Raton, FL: CRC Press.

Hartog, A., Frignet, B., Mackie, D., & Clark, M. (2014). Vertical seismic optical profiling on wireline logging cable. *Geophysical Prospecting*, *62*(4), 693–701.

Hecht, E. (1998). Optics 4th edition. optics. *Addison Wesley Longman Inc*, *1*, 1998.

Hohensinn, R., & Geiger, A. (2018). Stand-alone GNSS sensors as velocity seismometers: Real-time monitoring and earthquake detection. *Sensors*, *18*(11), 3712.

Hutt, C. R., Evans, J. R., Followill, F., Nigbor, R. L., & Wielandt, E. (2009). Guidelines for standardized testing of broadband seismometers and accelerometers. *US Geological Survey Open-File Report*, *1295*, 62.

IRIS-PASSCAL (2019). Sensor comparison chart. https://www.passcal.nmt.edu/content/instrumentation/sensors/sensor-comparison-chart

Jousset, P., Reinsch, T., Ryberg, T., Blanck, H., Clarke, A., Aghayev, R., et al. (2018). Dynamic strain determination using fibre-optic cables allows imaging of seismological and structural features. *Nature communications*, *9*(1), 2509.

Karrenbach, M., Cole, S., Ridge, A., Boone, K., Kahn, D., Rich, J., et al. (2018). Fiber-optic distributed acoustic sensing of microseismicity, strain and temperature during hydraulic fracturing. *Geophysics*, *84*(1), D11–D23.

Kechavarzi, C., Pelecanos, L., & Soga, K. (2019). Distributed fibre optic sensing for monitoring reinforced concrete piles. *Geotechnical Engineering Journal of the SEAGS & AGSSEA*, *50*(1), 43–51.

Kreger, S. T., Klein, J. W., Rahim, N. A. A., & Bos, J. J. (2015). Distributed Rayleigh scatter dynamic strain sensing above the scan rate with optical frequency domain reflectometry. In *Fiber optic sensors and applications xii*, *9480*, International Society for Optics and Photonics, pp. 948006.

Kuvshinov (2016). Interaction of helically wound fibre-optic cables with plane seismic waves. *Geophysical Prospecting*, *64*(3), 671–688.

Lay, T., & Wallace, T. C. (1995). *Modern global seismology* (Vol. 58). San Diego: Academic Press.

Lindsey, N. J., Martin, E. R., Dreger, D. S., Freifeld, B., Cole, S., James, S. R., et al. (2017). Fiber-optic network observations of earthquake wavefields. *Geophysical Research Letters*, *44*, 11–792. https://doi.org/10.1002/2017GL075722

Martin, E. R., Lindsey, N. J., Ajo-Franklin, J., & Biondi, B. (2018). Introduction to interferometry of fiber optic strain measurements. eartharxiv.org/jb2na

Masoudi, A., & Newson, T. P. (2016). Contributed review: Distributed optical fibre dynamic strain sensing. *Review of Scientific Instruments*, *87*(1), 011501.

Mateeva, A., Lopez, J., Potters, H., Mestayer, J., Cox, B., Kiyashchenko, D., et al. (2014). Distributed acoustic sensing for reservoir monitoring with vertical seismic profiling. *Geophysical Prospecting*, *62*(4), 679–692.

Mestayer, J., Cox, B., Wills, P., Kiyashchenko, D., Lopez, J., Costello, M., et al. (2011). Field trials of distributed acoustic sensing for geophysical monitoring, *Seg technical program expanded abstracts 2011* (pp. 4253–4257). Society of Exploration Geophysicists.

Munn, J. D., Coleman, T. I., Parker, B. L., Mondanos, M. J., & Chalari, A. (2017). Novel cable coupling technique for improved shallow distributed acoustic sensor VSPs. *Journal of Applied Geophysics*, *138*, 72–79.

Paitz, P., Sager, K., & Fichtner, A. (2018). Rotation and strain ambient noise interferometry. *Geophysical Journal International*, *216*(3), 1938–1952.

Papp, B., Donno, D., Martin, J. E., & Hartog, A. H. (2017). A study of the geophysical response of distributed fibre optic acoustic sensors through laboratory-scale experiments. *Geophysical Prospecting*, *65*(5), 1186–1204.

Parker, T., Shatalin, S., & Farhadiroushan, M. (2014). Distributed acoustic sensing—A new tool for seismic applications. *first break*, *32*(2), 61–69.

Posey, R, Johnson, G., & Vohra, S. (2000). Strain sensing based on coherent Rayleigh scattering in an optical fibre. *Electronics Letters*, *36*(20), 1688–1689.

Reinsch, T., Thurley, T., & Jousset, P. (2017). On the mechanical coupling of a fiber optic cable used for distributed acoustic/vibration sensing application a theoretical consideration. *Measurement Science and Technology*, *28*(12), 127003.

Rost, S., & Thomas, C. (2002). Array seismology: Methods and applications. *Reviews of Geophysics*, *40*(3), 2–1.

SEAFOM (2018). Measuring sensor performance document (SEAFOM MSP-02)—DAS parameter definitions and tests. https://seafom.com/?mdocs-file=1270

Schroeder, J. (1980). Brillouin scattering and Pockels coefficients in silicate glasses. *Journal of Non-Crystalline Solids*, *40*(1-3), 549–566.

Wang, H. F., Zeng, X., Miller, D. E., Fratta, D., Feigl, K. L., Thurber, C. H., & Mellors, R. J. (2018). Ground motion response to an Ml 4.3 earthquake using co-located distributed acoustic sensing and seismometer arrays. *Geophysical Journal International*, *213*(3), 2020–2036.

Wielandt, E., & Streckeisen, G. (1982). The leaf-spring seismometer: Design and performance. *Bulletin of the Seismological Society of America*, *72*(6A), 2349–2367.

Willis, M., Ajo-Franklin, J., & Roy, B. (2017). Introduction to this special section: Geophysical applications of fiber-optic distributed sensing. *The Leading Edge*, *36*(12), 973–974.

Yu, C., Zhan, Z., Lindsey, N. J., Ajo-Franklin, J. B., & Robertson, M. (2019). The potential of das in teleseismic studies: Insights from the Goldstone experiment. *Geophysical Research Letters*, *46*, 1320–1328. https://doi.org/10.1029/2018GL081195

Zeng, X., Lancelle, C., Thurber, C., Fratta, D., Wang, H., Lord, N., et al. (2017). Properties of noise cross-correlation functions obtained from a distributed acoustic sensing array at garner valley, california. *Bulletin of the Seismological Society of America*, *107*(2), 603–610.

Zhirnov, A., Fedorov, A., Stepanov, K., Nesterov, E., Karasik, V., Svelto, C., & Pnev, A. (2016). Effects of laser frequency drift in phase-sensitive optical time-domain reflectometry fiber sensors. arXiv preprint arXiv:1604.08854.

Zhou, J., Pan, Z., Ye, Q., Cai, H., Qu, R., & Fang, Z. (2013). Characteristics and explanations of interference fading of a ϕ-OTDR with a multi-frequency source. *Journal of lightwave technology*, *31*(17), 2947–2954.